Journal of Materials Chemistry A

ROYAL SOCIETY OF CHEMISTRY

PAPER

View Article Online
View Journal

Cite this: DOI: 10.1039/d1ta01818c

Ionophobic nanopores enhancing the capacitance and charging dynamics in supercapacitors with ionic liquids†

Zhongdong Gan,[ab] Yanlei Wang,*[bcd] Mi Wang,[bc] Enlai Gao,[e] Feng Huo,[bc] Weilu Ding,[bc] Hongyan He *[bcd] and Suojiang Zhang *[abc]

Nano-porous electrodes combined with ionic liquids (ILs) are widely favored to promote the energy density of supercapacitors. However, this is always accompanied by the reduced power density, especially considering the high viscosity and large steric hindrance of ILs. Here, we use computational simulations coupled with the equivalent circuit model to quantify the charging process and overall performance of the IL-based supercapacitor. We find that the ions in the electrode with ionophobic pores display a new charging mechanism under a threshold potential, namely co-ion adsorption, which has been ignored before. This identified abnormal charging process can not only efficiently enhance the differential capacitance but also remarkably speed up the charging dynamics. Meanwhile, the pores with various sizes and lengths in the electrode demonstrate the same tendency, reflecting the relative universality of the collaborative enhancement of the co-ion adsorption process. Furthermore, the quantitative relation between charging time/capacitance and electric voltage/ionophobic properties is further obtained to evaluate the critical conditions for synergistically improving the energy density and power density of supercapacitors. These findings may advance the understanding of charging mechanisms in porous electrodes and manifest that the ionophobicity is one important factor in the rational design of supercapacitors with ILs or other electrochemical devices in the field of chemical engineering.

Received 2nd March 2021
Accepted 7th May 2021

DOI: 10.1039/d1ta01818c

rsc.li/materials-a

Introduction

The development of advanced energy storage technology is of great importance due to the increasing shortage of fossil energy and the consequent environmental degradation.[1] Among storage approaches, the supercapacitor has attracted considerable attention in the academic and industrial field due to the outstandingly large power density, fast charge–discharge rate and long cycle life.[2–5] To enhance the energy density of a supercapacitor, the strategy of combining a nano-porous graphite electrode with high specific surface area and ionic liquid (IL) electrolytes with a wide electrochemical window has predominantly been adopted in the high performance supercapacitor.[6–9,64] For instance, the energy density of a supercapacitor composed of a nano-porous carbon electrode and IL electrolyte could reach as high as ~246 W h kg^{-1}, which is comparable to the common lithium batteries.[10,11] However, the IL-based supercapacitors exhibit a moderate power density and slow charging process because of the high viscosity and large ionic steric hindrance of the IL electrolyte, which prevents their development and commercial applications.[12]

Physically, the ion-transporting process within the nano-porous graphite and IL interface balancing the electronic charges dominates the electrochemical energy storage. To clarify the ionic transport mechanism and the correlation between the supercapacitor performance and electrical double layer (EDL) structure, plenty of studies have been conducted *via* experimental and theoretical methods.[13–17] Through NMR spectroscopy,[18,19] electrochemical quartz crystal microbalance (EQCM)[20] experiments and molecular dynamics (MD) simulations,[21] three basic charging mechanisms in supercapacitors have been found: the counter-ion adsorption, co-ion desorption and ion-exchange. Furthermore, Chmiola *et al.*[22,23] and Largeot *et al.*[24] found that the supercapacitors possessed the maximum differential capacitance when the size of pores and ions in the electrolyte was comparable, which was also proved by theoretical studies.[25–27] Feng *et al.*,[27] Jiang *et al.*,[26] and Wu *et al.*[25] even

[a]School of Chemical Engineering and Technology, Tianjin University, Tianjin, 300072, China

[b]Beijing Key Laboratory of Ionic Liquids Clean Process, State Key Laboratory of Multiphase Complex Systems, CAS Key Laboratory of Green Process and Engineering, Institute of Process Engineering, Chinese Academy of Sciences, Beijing 100190, China. E-mail: ylwang17@ipe.ac.cn; hyhe@ipe.ac.cn; sjzhang@ipe.ac.cn

[c]University of Chinese Academy of Sciences, Beijing 100049, China

[d]Innovation Academy for Green Manufacture, Chinese Academy of Sciences, Beijing 100190, China

[e]Department of Engineering Mechanics, School of Civil Engineering, Wuhan University, Wuhan, Hubei 430072, China

† Electronic supplementary information (ESI) available. See DOI: 10.1039/d1ta01818c

showed that the capacitance demonstrated an oscillatory behavior as the pore width varied owing to the interference of two electrical double layers near each wall. Hence, the interfacial structures and properties have a vital impact on the ionic transport mechanism and overall performance of the IL-based supercapacitor. Notably, almost all the previous studies focus on the ionophilic pores in electrodes, where ILs can enter the pore spontaneously. However, limited work has been devoted to understanding the quantitative correlation between ionophobicity/ionophility and the performances of supercapacitors, especially for the IL electrolyte.

The wettability of ILs at the electrodes can be precisely regulated from "ionophilic" to "ionophobic" *via* the molecular design of ions or grafting the electrodes with functional groups. Recently, Kondrat *et al.*[28] and Lian *et al.*[29] found that the ionophobicity of ILs can store more energy in the supercapacitor using the methods of the MFT (Mean-Field Theory) model and density functional theory (DFT) when the voltage is high. Qian *et al.*[30] showed that the "electrolyte-phobic surface" can enhance the energy density of batteries from experiments. Besides, the charging dynamics of ILs was expected to be much faster in the ionophobic pores than that in ionophilic pores.[31–34] Hence, this can be confirmed by the fact that the ionophobic interface can play a key role in enhancing the capacitance or the power density of supercapacitors. However, how the wettability, especially the ionophobic pore, affects the charging mechanism and further boosts the capacitance and charging dynamics of supercapacitor are not yet been clearly clarified, which are essential for both the rational design and efficient management of IL-based supercapacitors.

In this work, the relationship between supercapacitor performances and wettability is quantitatively revealed using the massive molecular dynamics (MD) simulations coupled with the constant potential method (CPM).[35] We find that the differential capacitance increases obviously as the pore changes from ionophilic to ionophobic in the high voltage zone. Meanwhile, a new charging mechanism of co-ion adsorption in ionophobic pores is proposed to clarify the intrinsic nature of the enhancing capacitance, which differs from the traditional ones described in previous studies.[18,36,37] Furthermore, the electrical resistance is predicted by the equivalent circuit model, showing the accelerating charging dynamics for supercapacitors with the ionophobic pores. Based on these findings, the implication of the ionophobic interface was discussed and proposed in the design of new efficient IL-based devices including supercapacitors, batteries, electrical reduction cells, and so on.

Computational models and methods

Details of molecular dynamics simulation

The supercapacitor composed of 1-ethyl-3-methylimidazolium tetrafluoroborate ($EmimBF_4$) and a nanoporous graphite electrode was constructed as shown in Fig. 1a, where five parallel graphenes with a single pore were assembled to form one electrode. $EmimBF_4$, as a typical type of ILs, has been extensively used in plenty of simulations and experimental works

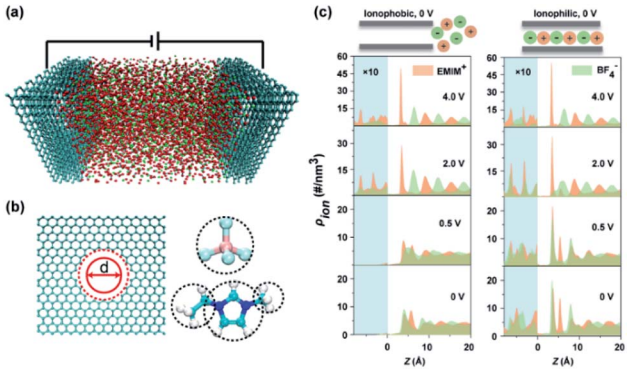

Fig. 1 Schematic of the molecular simulation setup of the supercapacitor. (a) A snapshot of the simulation cell consisting of the nanoporous graphite electrode and ILs. (b) The atomic structure of graphene with the single pore and the representation of the coarse-grained model of $EmimBF_4$ ILs. (c) The number density distribution at different potentials in ionophobic and ionophilic electrodes. The blue shaded region ($Z < 0$) is the in-pore region, where the number density is magnified 10 times for clarification.

before.[38–41] The size of the electrode was 6.72×6.79 nm^2 while the thickness of ILs varied from 7.9 to 8.3 nm (1400 ion pairs), where the thickness was large enough to reproduce a bulk state of ILs in the central region of the system. The diameter (d_{pore}) of the pore in graphene was set as 0, 0.98, 1.62, 2.46, and 3.3 nm, where d_{pore} was defined as the incircle diameter of the hexagonal hole subtracting the vdW diameter of carbon. A two-dimensional supercell was used with periodic boundary conditions along with the IL-electrode interface and open boundary conditions were used in the direction across the electrode.

The coarse-grained force field was adopted for graphene and $EmimBF_4$ (Fig. S1(b)†),[42,43] both of which have been proved to be accurate enough to capture the thermodynamic and dynamic properties of graphene and ILs and describe the interface between them. The nonbonding interaction between the electrode and ILs consisted of coulombic and van der Waals (vdW) terms, where the cutoff distance for them was set as 1.5 nm. The coulombic interaction was computed using the particle–particle–particle–mesh (PPPM) method,[44] while the vdW interaction was described by the Lennard-Jones potential,

$$V(r) = 4\varepsilon\left[\left(\frac{\sigma}{r}\right)^{12} - \left(\frac{\sigma}{r}\right)^{6}\right] \quad (1)$$

where ε was the energy parameter between ILs and graphene. The value of ε was altered in the present work to generate the electrode with different wettability from ionophilic to ionophobic. All the simulations were performed *via* a large-scale atomic/molecular massively parallel simulator (LAMMPS).[45] The timestep in the simulation was 2 fs. The external electrical potential between the two electrodes was added *via* the CPM, in which the charges on the electrode atoms were described as a Gaussian function, allowing the fluctuations of charges during the simulation.[15,46] The Gaussian function parameter for the graphene electrode was set to 1.979 Å^{-1}.[47] The hybrid system at different voltages was first equilibrated for at least 40 ns at

300 K in an NVT ensemble. Then a continuous 10 ns-long simulation was performed to track the position of ions and the charging state of the electrode.

Calculation of the differential capacitance and equivalent circuit model

The areal differential capacitance (C_d) is a measure of how the EDL microstructure responds to electrical potential perturbations caused by a variation in the electric potential, which can be calculated *via* $C_d = dQ/dU_{RPZC} = dQ/d(U_{elec} - U_{PZC})$. Q is the areal charge density in the electrode, U_{RPZC}, U_{elec} and U_{PZC} are the relative electrode potential, electrode electrical potential applied in the simulation and the potential of zero charge, respectively. An equivalent circuit, normally used to approximate the impedance data, was an electric circuit made up of the basic elements such as resistance and capacitance in a simple arrangement.[48] We employed the commonly used transmission line to represent the supercapacitor with the nano-porous graphite electrode and ILs (ESI Note S1†), in which the charge gradually penetrates the electrode, to model the equivalent circuit.[49]

Results and discussion

Enhancing the differential capacitance of the supercapacitor with ionophobic pores

The wettability of ILs at the nano-porous graphite arises from the interfacial adhesion energy, which can be regulated *via* rescaling the coupling strength of the IL-electrode interface. The coupling strength can be measured *via* $\eta_{ion} = \varepsilon/\varepsilon_0$, where ε and ε_0 are the regulated and initial energy parameter between the electrode and the ionic liquids in the Lennard-Jones function. Tuning the coupling strength, one can construct the electrode pore with different wettability as shown in Fig. 1 & S2(a),† where the ionophobic pore represents that ILs cannot enter the pore spontaneously. As shown in Fig. S2(a),† the smaller the value of the coupling strength, the more the ionophobic degree of the pore as the ion number density is much smaller than that in the bulk, for example, $\eta_{ion} > 0.7$ and $\eta_{ion} < 0.7$ represent the ionophilic pore and ionophobic pore, respectively. The effect of wettability on the interfacial ILs was further measured by the number density distribution of the cation and anion as shown in Fig. 1c. The peak of the surface adsorbed cation layer ($z \sim 4$ Å) for the ionophobic electrode is weaker than that for the ionophilic one, and there are no ILs in the ionophobic pore when U_{elec} is low. However, the motivating force generated from the large U_{elec} can pull the ions into the ionophobic pore, showing an obvious structural transition during the charging process.

The sparse distribution and structural transition of interfacial ILs in the supercapacitor with ionophobic pores indicate that the charging process and capacitive performance are sensitive to the pore wettability. The areal differential capacitance can be calculated through the relation between the charge density and relative electrode potential as shown in Fig. 2a & S3.†[50,51] For the ionophilic case, C_d of the slab electrode with η_{ion} = 1.0 is 4.68 μF cm^{-2} when U_{elec} = 2.0 V, which is close to the previous theoretical and experimental results (Table S2†),[52–59] showing the rationality of simulation adopted herein. Comparing C_d of the electrodes with various wettability, a critical voltage (U_C = 2.0 V) can be determined. When U_{elec} is less than U_C, both C_d of the supercapacitor with ionophilic and ionophobic pores increase gradually with U_{RPZC}, while C_d of that with weakly ionophobic pores fluctuates around ~5.0 μF cm^{-2} as U_{RPZC} increases. Once the U_{RPZC} is beyond U_C, both C_d of the supercapacitor with ionophilic and weakly ionophobic pores decreases significantly with U_{RPZC}; however, C_d of that with ionophobic pores shows a less significant fall. Consequently, C_d for the supercapacitor with ionophobic pores will be larger than that with the ionophilic pores, especially when $U_{elec} > 2.0$ V.

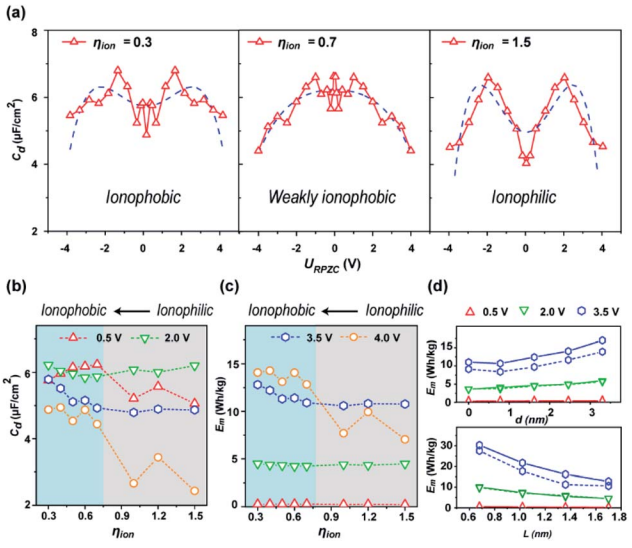

Fig. 2 The wettability and geometry dependent differential capacitance. (a) The differential capacitance as a function of the electric voltage for the supercapacitor with ionophobic, weakly ionophobic and ionophilic pores (d_{pore} = 2.46 nm). (b and c) The differential capacitance and energy density (U_{elec} = 0.5, 2.0, 3.5 and 4.0 V) as a function of the relative energy between ILs and the graphite electrode. (d) The energy density (U_{elec} = 0.5, 2.0, and 3.5 V) as a function of the pore size and pore length. The solid and dashed lines represent the ionophobic and ionophilic electrode, respectively.

Furthermore, the capacitance and mass energy density (E_m) at typical U_{elec} (0.5, 2.0, 3.5 and 4.0 V) were correlated with the wettability as shown in Fig. 2b and c. Interestingly, C_d shows an obvious increase as η_{ion} decreases, especially at a large voltage. For instance, when η_{ion} decreases from 1.5 to 0.3, C_d increases by about 13.8% and 100% for U_{RPZC} = 0.5 and 4.0 V, respectively. As a result, a much higher energy density can be achieved for the supercapacitor with ionophobic electrodes.

The enhancement tendency can also be confirmed from the increasing specific charge density in electrodes as shown in Table S3.† Porous structures including the pore size (d) and length (L) may have great impacts on the capacitance and energy density (Fig. 2d & S4†). One can find that C_d increases with d, while it almost stays steady when L varies. Consequently, E_m of the supercapacitor increases with d and decreases with L.

It should be noted that the capacitance in our model includes two contributions, the wall surface capacitance and the pore surface capacitance, indicating that the total capacitance is not only related with the pore size but also concerned with the wall surface area. Interestingly, for all supercapacitors, both C_d and E_m for the electrode with ionophobic pores are larger than they are for the ionophilic one, which is consistent with the results discussed above. These results suggest that the electrode with ionophobic pores will be favorable for the supercapacitor with higher differential capacitance and energy density.

"Co-ion adsorption" mechanism in the charging process of the supercapacitor with ionophobic pores

The enhanced capacitance of the supercapacitor with ionophobic pores should arise from the unique charging process of ILs in the nanopore. The charging mechanism of nanopores could be understood by analyzing the variations of the in-pore population of ions. In Fig. 3a, the ionophilic pores can be easily wetted by ILs, and the number density of in-pore cation/anion characters shows a nearly linear change as U_{elec} increases. The in-pore population of counterions in the ionophobic pore also increases with U_{elec}, whose dependence is similar to that in the ionophilic pore. However, the in-pore population of co-ions with ionophobic pores ($Emim^+$ at the positive electrode or BF_4^- at the negative electrode) will increase first and then decrease, overturning at the critical potential of ~2.0 V. For example, the in-pore population of $Emim^+$ at the positive ionophilic electrode ($\eta_{ion} = 1.0$) decreases from 4.3 to 3.9 #/nm^{-3} while that at the ionophobic electrode increases ($\eta_{ion} = 0.3$) from 0 to 3.0 #/nm^{-3} as U_{elec} ranges from 0 to 2 V. Similarly, the same trend is also found in ionophobic electrodes with different pore sizes and pore lengths as displayed in Fig. S5,† where the in-pore anion populations in different pore sizes and lengths all go through an increasing trend at the negative electrode, which can be attributed to co-ion adsorption in the charging process. The fully opposite trend of the in-pore population of ions in the ionophobic and ionophilic pores indicates that the dominant charging mechanism should be different.

In general, the charging mechanism can be quantitatively measured by the parameter (X) as follows,[36]

$$X = \frac{N - N_0}{(N^{counter} - N^{co}) - (N_0^{counter} - N_0^{co})}$$

where N and N_0 are the total number of in-pore ions at a certain U_{elec} and null potential. $N^{counter}$ and N^{co} are the corresponding in-pore number of counter- and co-ions. In general, three different classical charging mechanisms were identified from X, where $X = 1$, 0, and -1 represents the pure counterion adsorption, ion-exchange and co-ion desorption, respectively. For the ILs in the supercapacitor with ionophilic pores, all X equals zero at different U_{elec} (Fig. S6†), which is consistent with the unchanged ion population inside the pore discussed above. In contrast, for the ionophobic electrode, both the classical counterion adsorption and abnormal "co-ion adsorption" process exist in the charging process (Fig. 3b), which is completely different from the traditional viewpoint.[18–20,36]

The value of X for the ionophobic pore is also far beyond 1.0 (Fig. S6(b)†), showing the new different charging mechanisms again, for instance, X ($U_{elec} = 1.0$ V) equals to 2.0, 6.0 and 6.6 when $\eta_{ion} = 0.3$, 0.5 and 0.6, respectively. When U_{elec} is beyond the critical voltage, the in-pore population of ions falls into the same trend as the ionophilic pores and displays a prime ion-exchange charging mechanism when the applied voltage becomes higher. The abnormal "co-ion adsorption" process can make more co-ions enter into the nanopore and finally lead to the enhanced capacitance as discussed in Fig. 2.

To understand the commencing of the abnormal co-ion adsorption process, the steered MD simulations were further

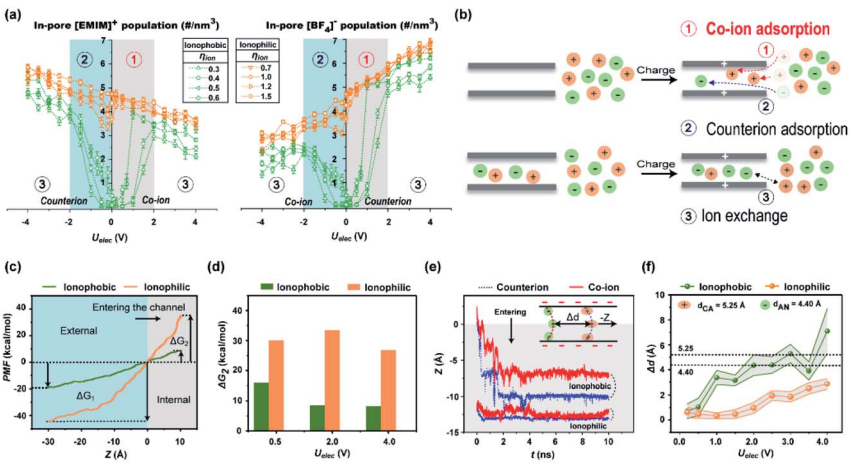

Fig. 3 The new charging mechanism of "co-ion adsorption". (a) In-pore cation and in-pore anion population at different electrodes as a function of the electrical voltage. (b) Illustrations of three different charging mechanisms. (c) Potential of mean force (PMF) for the co-ion ($Emim^+$) entering the positive electrode with ionophobic ($\eta_{ion} = 0.3$) and ionophilic ($\eta_{ion} = 1.0$) pores at 2.0 V. (d) The energy barrier for the co-ion entering the pore with different wettability. (e) The evaluation of the position of the forefront of ILs confined in the pore, where the negative electrode at 1.5 V was shown as an example. (f) Average equilibrium gap between counter-ions and co-ions when entering the negative ionophobic and ionophilic pores.

performed, computing the potential of mean force (PMF) of the co-ion entering the ionophilic or ionophobic pore (Fig. 3c and d). The entering and exporting barriers of the co-ion were respectively calculated. Both barriers for the ionophobic pore are far smaller than that in the ionophilic one, demonstrating the feasibility of the co-ion entering the ionophobic pore. The small barriers should be attributed to the weak nature of the vdW term in ionophobic pores (Fig. S7†), where the repulsive force from the ionophobic electrode is weaker than the binding force within the cation–anion pair. That is to say, the correlation between cations and anions is strong for ILs in the ionophobic surface when U_{elec} is less than U_C. The small barrier means that the abnormal "co-ion adsorption" process is much more likely to happen in ionophobic pores. Meanwhile, the entering depth of the co-ion is smaller than that of the counter-ion in the ionophobic pore (Fig. 3e and f). The gap between the depth of the counterion and co-ion for the ionophobic pore increases from 0.1 to 0.45 nm as U_{elec} increases (close to the diameter of $Emim^+$ and BF_4^-), which is far larger than that in the ionophilic pore. The evolution of the gap suggests that the co-ion is dragged into the pore by the counterions. Hence, all the entering barriers, wetting depth and the ion-electrode interface agree well with each other, revealing the physics behind the abnormal "co-ion adsorption" in the ionophobic pores.

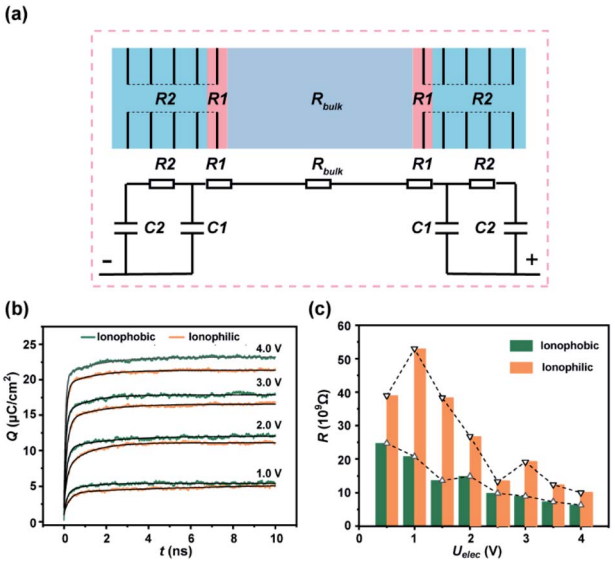

Fig. 4 The accelerating charging dynamics of the supercapacitor with the ionophobic electrode. (a) Equivalent electric circuit used to model our simulation setup. (b) The charging process of the electrode with ionophobic and ionophilic pores as a function of time when finite potentials are applied. (c) The total electric resistance of the electrode with ionophobic and ionophilic pores (d_{pore} = 2.46 nm) at different applied potentials.

Accelerating charging dynamics of the supercapacitor with ionophobic pores

From the in-pore population of ions shown in Fig. 3a, a rapid change of the co-ion and counter-ion occurred at the low voltage for the ionophobic supercapacitor, suggesting that the ionophobic pore exhibits faster charge dynamics compared with the ionophilic pore. The accelerated charging process is consistent with the previous theoretical prediction based on the MFT.[32] The charging dynamics not only depends on the IL electrolyte but also the surface of the pore in the electrode, which can be quantitatively measured by the equivalent circuit model.[49,60] Such an equivalent circuit is composed of a series of capacitors storing charge through the polarization of ILs and resistances expressing the dissipation when ILs migrate across the pores, linking the nanoscale MD simulation with the macroscopic performance.

Considering the setup of the supercapacitor in the present work and the different contacting environment of the outermost layer and the other four layers, the network structure of electric capacitors (C_1 and C_2) and electric resistances (R_1, R_2, and R_{bulk}) are illustrated in Fig. 4a, and the calculation was present in ESI Note S1.† C_1 and C_2 are the differential capacitances of the two electrodes. R_{bulk}, R_1 and R_2 are the resistances of the IL electrolyte and the nanoporous electrode ($R_2 = 4R_1$), which can be determined by fitting the charge density at the electrode surface *versus* time following the charge equation,[60]

$$Q(t) = Q_{max}\left[1 - A_1 \exp\left(-\frac{t}{\tau_1}\right) - A_2 \exp\left(-\frac{t}{\tau_2}\right)\right] \quad (2)$$

where Q_{max} is the convergent charge density, τ_1 and τ_2 are the relaxed time parameter, and A_1 and A_2 are the fitting parameters. Furthermore, the non-equilibrium MD simulations were conducted by applying a different voltage to obtain the evaluation of the charge state along time (Fig. 4b). The results show that all the charging curves for ionophobic and ionophilic supercapacitors can be fitted well using the above charge equation.

From the equivalent circuit model, the total resistance of the overall electrode ($R_1 + R_2$) and the corresponding resistivity can be obtained as shown in Fig. 4c and S8,† respectively. The fact can be found that the total resistance of ionophobic electrodes at all ranges of voltage is smaller than that of the ionophilic one. For instance, ($R_1 + R_2$) at 0.5 V for the ionophobic and ionophilic electrodes are ~24 and 39 GΩ, respectively. The total electric resistance is much larger than that of the bulk resistance (0.073 GΩ) which indicates that ion transport of ILs in nanoconfinement is slower than that in the bulk phase. Besides, a crude estimate of the charging time can be determined from our simulation using an effective macroscopic model,[60]

$$\tau_{macro} = R \times C \times \left(\frac{L_{macro}}{L_{sim}}\right)^2 \quad (3)$$

where C and R are the total capacitance and electric resistance of the electrodes and L_{sim} and L_{macro} are the thickness of the electrode in the simulation and macroscale. For a typical commercial supercapacitor, the electrode size is about L_{macro} = 100 μm, which gives us characteristic charging times ranging between 10 and 300 s for our systems. The obtained charging time is in the same order of that in ref. 53 and 24 (about 20 s), reflecting the rationality of the calculation adopted herein. Comparing the ionophobic and ionophilic cases, the charging

time of the ionophilic electrode can be an order of magnitude larger than that in the ionophobic electrode. For example, the charging time is about 23 s and 115 s in ionophobic ($\eta_{ion} = 0.3$) and ionophilic ($\eta_{ion} = 1.0$) electrodes at 2.0 V, respectively.

The lower electric resistance suggests that the ionophobic pore can promote the charging process, which agrees well with the previous study[33] based on the narrow cylinder pore using the MFT model. Accelerating charging dynamics should be attributed to the empty ionophobic pore at null potential. Once the external voltage is imposed, the "co-ion adsorption" and counterion adsorption occur simultaneously at the initial stage. The consistent moving direction and low wettability will weaken the IL-wall friction, lead to faster charging dynamics, and finally reduce the overall resistance of the ionophobic electrode. As the voltage increases, more and more ions are accommodated in the nanopore, which further blocks the entry of the ions and approaches the charging process in the ionophilic pores. Such faster-charging dynamics in ionophobic pores will greatly benefit the IL-based nanoporous supercapacitors as the ion transport of ILs is often a disadvantage due to their high viscosity. We therefore believe that ionophobic pores present an exciting opportunity to address the challenge of slow charging dynamics in IL-based supercapacitors or other power devices.

Additional discussion

In general, ionophilic electrodes featuring sub-nanopores are always used to enhance the energy density of the supercapacitor. However, there still exist several challenges that need to be confronted from the practical point of view. First, sub-nanopores tend to lower the power density of supercapacitors and nanoconfinement is slower than that in the bulk, especially for the ILs with high viscosity.[61,62] Second, the charging process in narrow ionophilic pores is always accompanied by overfilling,[32] and it will go through further deterioration especially when conducting the cyclic recharging.[63] Third, ionophilic electrodes would have significant intakes of electrolytes, which will reduce the energy density and increase the cost.[30] Resolving these issues, ionophobic electrodes are proposed in this work, which will not only enhance the energy density but also boost the charging dynamics.

As shown in Fig. 5, it gives the information of mass energy density and charging time estimated by formula (3) ($1/\tau_{macro}$) of supercapacitors with different ionophobic or ionophilic electrodes. The ionophobic electrodes are always characterised with a smaller charging time at all imposed potentials. Furthermore, the more ionophobic the electrode is, the shorter charging time it will have. As the coupling strength increases from 0.3 (ionophobic) to 1.5 (ionophilic), the mass energy density decreases from 15.7 to 12.5 W h kg^{-1} while the charging time increases from 10 to 39 s, demonstrating the collaborative enhancement of the performance of supercapacitors. The enhancement will be sharper for the ionophobic supercapacitor in the high potential zone (U_{elec} > 2.0 V). That is to say, the ionophobic approach should be especially important to the development of the high voltage supercapacitor.

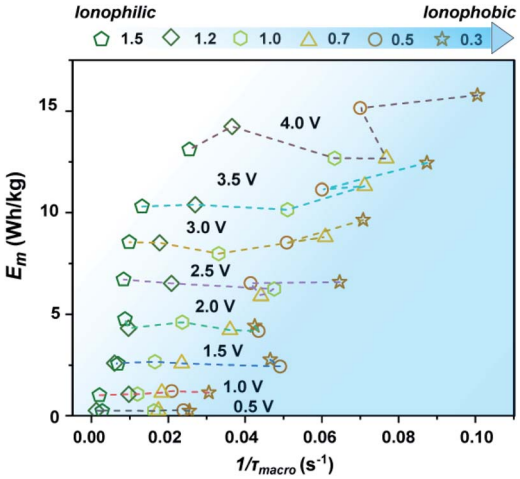

Fig. 5 The mass energy density *versus* reciprocal charging time of supercapacitors. The porous electrodes with coupling strength ranging from 0.3 (ionophobic) to 1.5 (ionophilic) at different voltages are considered in this plot.

The collaborative enhancement of mass energy density and charging dynamics should be attributed to the abnormal ion transport mechanism, co-ion adsorption. The co-ion adsorption process should be the unique feature of the IL-based electrolyte and the ionophobic electrode. The ionophobic electrode can weaken the interaction strength between the electrode and co-ions, while the special hydrogen bond (Z bond) between cations and anions in ILs leads to a strong ionic correlation. The strong cation–anion correlation, which surpasses the repulsive interaction caused by co-ion-electrode interaction and the external electrode electric potential, makes the co-ions enter the ionophobic pore and enhances the image charge of the electrode, giving rise to the co-ion adsorption in the low voltage zone and further enhancing the mass energy density. Many other factors can also affect the overall performance of the IL-based supercapacitor, such as the type of cations and anions, material properties (surface roughness, conductivity, and thermal expansion coefficient), the combination of different kinds of ionic liquids, and so on. However, we believe that the ionophobic term will still be an important term for the rational design and management of the supercapacitor, particularly the high voltage one. Moreover, the quantitative relation between the differential capacitance, mass energy density, ionic transport resistance and the ionic ionophobic degrees or interfacial coupling strength suggests that we could enhance the supercapacitor performance by the surface modification of the electrode (such as MXene and its functionalized structures) or molecular design of the IL electrolyte.

Conclusions

In summary, we have quantitively investigated the effects of ionophobicity on the stored energy and charging dynamics of supercapacitors *via* performing MD simulations. The capacity results show that the ionophobicity prolongs the high capacitance area to the high voltage region, leading to the

enhancement of energy density at high electrical potential, which is also true for electrodes with different geometries. Referring to the ion population in different pores, a new charging process, "co-ion adsorption", was proposed in ionophobic pores when the potential was below a certain threshold potential, which has not been explored in previous works. Verified by the steered MD simulation results and the entering depth of ions, we concluded that the emerging co-ion adsorption process was on account of the strong electrostatic cation–anion attraction surpassing the unfavorable interaction between the co-ion and applied potential (including the electrostatic repulsion and the ionophobic repulsion). Additionally, from the ion transport resistances obtained by the equivalent circuit model, charging dynamics in ionophobic systems is much faster compared to the ionophilic systems, especially in the range of low potential due to the smaller friction generated in ionophobic pores when the co-ion adsorption commences. By regulating the interactions of the electrolyte–electrode, we have revealed a new charging mechanism of co-ion adsorption and found a better and faster way to store energy in supercapacitors.

Conflicts of interest

There are no conflicts to declare.

Acknowledgements

This work was supported by the National Natural Science Foundation of China (21922813, 22078322, 21890762 and 21776278), Innovation Academy for Green Manufacture, Chinese Academy of Sciences (IAGM2020C16), and the Youth Innovation Promotion Association of CAS (2017066 and 2021046).

Notes and references

1 J. Motavalli, *Nature*, 2015, **526**, S96–S97.
2 J. R. Miller and P. Simon, *Science*, 2008, **321**, 651–652.
3 P. Simon and Y. Gogotsi, *Nat. Mater.*, 2008, **7**, 845–854.
4 P. Naskar, A. Maiti, P. Chakraborty, D. Kundu, B. Biswas and A. Banerjee, *J. Mater. Chem. A*, 2021, **9**, 1970–2017.
5 L. Yan, J. Huang, X. Dong, Z. Guo, Z. Wang and Y. Wang, *J. Mater. Chem. A*, 2020, **8**, 15051–15057.
6 K. Dong, X. Liu, H. Dong, X. Zhang and S. Zhang, *Chem. Rev.*, 2017, **117**, 6636–6695.
7 M. V. Fedorov and A. A. Kornyshev, *Chem. Rev.*, 2014, **114**, 2978–3036.
8 S. Zhang, Y. Wang, H. He, F. Huo, Y. Lu, X. Zhang and K. Dong, *Green Energy Environ.*, 2017, **2**, 329–330.
9 B. Li, C. Wang, Y. Zhang and Y. Wang, *Green Energy Environ.*, 2020, DOI: 10.1016/j.gee.2020.04.009.
10 H. Yang, S. Kannappan, A. S. Pandian, J.-H. Jang, Y. S. Lee and W. Lu, *Nanotechnology*, 2017, **28**, 445401.
11 C. H. Kim, J.-H. Wee, Y. A. Kim, K. S. Yang and C.-M. Yang, *J. Mater. Chem. A*, 2016, **4**, 4763–4770.
12 L. Miao, H. Duan, Z. Wang, Y. Lv, W. Xiong, D. Zhu, L. Gan, L. Li and M. Liu, *Chem. Eng. J.*, 2020, **382**, 122945.
13 A. A. Lee, D. Vella, A. Goriely and S. Kondrat, *Phys. Rev. X*, 2016, **6**, 021034.
14 R. Burt, K. Breitsprecher, B. Daffos, P.-L. Taberna, P. Simon, G. Birkett, X. S. Zhao, C. Holm and M. Salanne, *J. Phys. Chem. Lett.*, 2016, **7**, 4015–4021.
15 J. Vatamanu, M. Vatamanu and D. Bedrov, *ACS Nano*, 2015, **9**, 5999–6017.
16 M. Beidaghi and Y. Gogotsi, *Energy Environ. Sci.*, 2014, **7**, 867–884.
17 C. Merlet, B. Rotenberg, P. A. Madden, P. L. Taberna, P. Simon, Y. Gogotsi and M. Salanne, *Nat. Mater.*, 2012, **11**, 306–310.
18 A. C. Forse, J. M. Griffin, C. Merlet, J. Carretero-Gonzalez, A.-R. O. Raji, N. M. Trease and C. P. Grey, *Nat. Energy*, 2017, **2**, 16216.
19 A. C. Forse, J. M. Griffin, C. Merlet, P. M. Bayley, H. Wang, P. Simon and C. P. Grey, *J. Am. Chem. Soc.*, 2015, **137**, 7231–7242.
20 J. M. Griffin, A. C. Forse, W. Y. Tsai, P. L. Taberna, P. Simon and C. P. Grey, *Nat. Mater.*, 2015, **14**, 812–819.
21 L. Xing, J. Vatamanu, O. Borodin and D. Bedrov, *J. Phys. Chem. Lett.*, 2013, **4**, 132–140.
22 J. Chmiola, C. Largeot, P. L. Taberna, P. Simon and Y. Gogotsi, *Angew. Chem., Int. Ed.*, 2008, **47**, 3392–3395.
23 J. Chmiola, G. Yushin, Y. Gogotsi, C. Portet, P. Simon and P. L. Taberna, *Science*, 2006, **313**, 1760–1763.
24 C. Largeot, C. Portet, J. Chmiola, P. L. Taberna, Y. Gogotsi and P. Simon, *J. Am. Chem. Soc.*, 2008, **130**, 2730–2731.
25 P. Wu, J. Huang, V. Meunier, B. G. Sumpter and R. Qiao, *ACS Nano*, 2011, **5**, 9044–9051.
26 D.-e. Jiang, Z. Jin and J. Wu, *Nano Lett.*, 2011, **11**, 5373–5377.
27 G. Feng and P. T. Cummings, *J. Phys. Chem. Lett.*, 2011, **2**, 2859–2864.
28 S. Kondrat and A. A. Kornyshev, *Nanoscale Horiz.*, 2016, **1**, 45–52.
29 C. Lian, H. Liu, D. Henderson and J. Wu, *J. Phys.: Condens. Matter*, 2016, **28**, 414005.
30 C. Qian, J. Zhao, Y. Sun, H. R. Lee, L. Luo, M. Makaremi, S. Mukherjee, J. Wang, C. Zu, M. Xia, C. Wang, C. V. Singh, Y. Cui and G. A. Ozin, *Nano Lett.*, 2020, **20**, 7455–7462.
31 S. Kondrat and A. Kornyshev, *J. Phys. Chem. C*, 2013, **117**, 12399–12406.
32 S. Kondrat, P. Wu, R. Qiao and A. A. Kornyshev, *Nat. Mater.*, 2014, **13**, 387–393.
33 A. A. Lee, S. Kondrat, G. Oshanin and A. A. Kornyshev, *Nanotechnology*, 2014, **25**, 315401.
34 T. Mo, S. Bi, Y. Zhang, V. Presser, X. Wang, Y. Gogotsi and G. Feng, *ACS Nano*, 2020, **14**, 2395–2403.
35 Z. Wang, Y. Yang, D. L. Olmsted, M. Asta and B. B. Laird, *J. Chem. Phys.*, 2014, **141**, 184102.
36 A. C. Forse, C. Merlet, J. M. Griffin and C. P. Grey, *J. Am. Chem. Soc.*, 2016, **138**, 5731–5744.
37 J. M. Griffin, A. C. Forse, H. Wang, N. M. Trease, P.-L. Taberna, P. Simon and C. P. Grey, *Faraday Discuss.*, 2014, **176**, 49–68.

38 S.-W. Park, A. D. DeYoung, N. R. Dhumal, Y. Shim, H. J. Kim and Y. Jung, *J. Phys. Chem. Lett.*, 2016, **7**, 1180–1186.
39 C. Lian, K. Liu, K. L. Van Aken, Y. Gogotsi, D. J. Wesolowski, H. L. Liu, D. E. Jiang and J. Z. Wu, *ACS Energy Lett.*, 2016, **1**, 21–26.
40 Y. Shim and H. J. Kim, *ACS Nano*, 2010, **4**, 2345–2355.
41 C. Liu, Z. Yu, D. Neff, A. Zhamu and B. Z. Jang, *Nano Lett.*, 2010, **10**, 4863–4868.
42 C. Merlet, B. Rotenberg, P. A. Madden, P.-L. Taberna, P. Simon, Y. Gogotsi and M. Salanne, *Nat. Mater.*, 2012, **11**, 306–310.
43 L. Ruiz, W. Xia, Z. Meng and S. Keten, *Carbon*, 2015, **82**, 103–115.
44 R. W. Hockney and J. W. Eastwood, *Computer simulationusing particles*, Taylor & Francis, Inc., 1988.
45 S. Plimpton, *J. Comput. Phys.*, 1995, **117**, 1–19.
46 S. Bi, H. Banda, M. Chen, L. Niu, M. Chen, T. Wu, J. Wang, R. Wang, J. Feng, T. Chen, M. Dincă, A. A. Kornyshev and G. Feng, *Nat. Mater.*, 2020, **19**, 552–558.
47 S. K. Reed, O. J. Lanning and P. A. Madden, *J. Chem. Phys.*, 2007, **126**, 084704.
48 N. Jaffrezic-Renault, in *Encyclopedia of Interfacial Chemistry*, ed. K. Wandelt, Elsevier, Oxford, 2018, pp. 241–247, DOI: 10.1016/b978-0-12-409547-2.13489-4.
49 P. L. Taberna, P. Simon and J. F. Fauvarque, *J. Electrochem. Soc.*, 2003, **150**, A292.
50 N. Georgi, A. A. Kornyshev and M. V. Fedorov, *J. Electroanal. Chem.*, 2010, **649**, 261–267.
51 M. Sha, Q. Dou, F. Luo, G. Zhu and G. Wu, *ACS Appl. Mater. Interfaces*, 2014, **6**, 12556–12565.
52 E. Paek, A. J. Pak and G. S. Hwang, *J. Electrochem. Soc.*, 2012, **160**, A1–A10.
53 J. Vatamanu, O. Borodin, D. Bedrov and G. D. Smith, *J. Phys. Chem. C*, 2012, **116**, 7940–7951.
54 J. Vatamanu, O. Borodin and G. D. Smith, *J. Am. Chem. Soc.*, 2010, **132**, 14825–14833.
55 J. Vatamanu, O. Borodin and G. D. Smith, *J. Phys. Chem. B*, 2011, **115**, 3073–3084.
56 J. Xia, F. Chen, J. Li and N. Tao, *Nat. Nanotechnol.*, 2009, **4**, 505–509.
57 H. Ji, X. Zhao, Z. Qiao, J. Jung, Y. Zhu, Y. Lu, L. L. Zhang, A. H. MacDonald and R. S. Ruoff, *Nat. Commun.*, 2014, **5**, 3317.
58 E. Uesugi, H. Goto, R. Eguchi, A. Fujiwara and Y. Kubozono, *Sci. Rep.*, 2013, **3**, 1595.
59 C. Merlet, M. Salanne and B. Rotenberg, *J. Phys. Chem. C*, 2012, **116**, 7687–7693.
60 C. Péan, C. Merlet, B. Rotenberg, P. A. Madden, P.-L. Taberna, B. Daffos, M. Salanne and P. Simon, *ACS Nano*, 2014, **8**, 1576–1583.
61 A. Brandt, S. Pohlmann, A. Varzi, A. Balducci and S. Passerini, *MRS Bull.*, 2013, **38**, 554–559.
62 S. Kondrat, C. Pérez, V. Presser, Y. Gogotsi and A. Kornyshev, *Energy Environ. Sci.*, 2012, **5**, 6474–6479.
63 A. A. Lee, S. Kondrat and A. A. Kornyshev, *Phys. Rev. Lett.*, 2014, **113**, 048701.
64 Z. Lu, X. Xu, Y. Chen, X. Wang, L. Sun and K. Zhuo, *Green Energy Environ.*, 2020, **5**, 69–75.

Supporting Information for

Ionophobic nanopore enhancing capacitance and charging dynamics in supercapacitor with ionic liquids

Zhongdong Gan[a,b], Yanlei Wang[b,c,], Mi Wang[b,c], Enlai Gao[e], Feng Huo[b,c], Weilu Ding[b,c], Hongyan He[b,c,d,*] and Suojiang Zhang[a,b,c,*]*

[a]School of Chemical Engineering and Technology, Tianjin University, Tianjin, 300072 China

[b]Beijing Key Laboratory of Ionic Liquids Clean Process, State Key Laboratory of Multiphase Complex Systems, CAS Key Laboratory of Green Process and Engineering, Institute of Process Engineering, Chinese Academy of Sciences, Beijing 100190, China

[c]University of Chinese Academy of Sciences, Beijing 100049, China

[d]Innovation Academy for Green Manufacture, Chinese Academy of Sciences, Beijing 100190, China

[e]Department of Engineering Mechanics, School of Civil Engineering, Wuhan University, Wuhan, Hubei 430072, China

Corresponding Authors:

Email: ylwang17@ipe.ac.cn (Y. Wang); hyhe@ipe.ac.cn (H. He); sjzhang@ipe.ac.cn (S. Zhang)

Supporting Tables:

Table S1. Interface Energy of $EMIMBF_4$-Grapheen with different VDW interactions

η_{ion}	0.3	0.4	0.5	0.6
Γ (J/m^2)	1.678	0.975	-0.052	-0.854
η_{ion}	0.7	1.0	1.2	1.5
Γ (J/m^2)	-1.526	-3.985	-5.636	-8.176

Table S2. Differential Capacitances of computational and experimental results.[1-8]

Electrode material	Electrolyte	Capacitance ($\mu F/cm^2$)	Reference
Planar graphene	[BMIM] [PF_6]	4.8	[1] MD
Graphite	[$C_n$mim] [TFSI]	5.5	[2] MD
3-layer graphene	[pyr_{13}] [TFSI]	4.8	[3] MD
2-layer graphene	[pyr_{13}] [FSI]	5.0	[4] MD
1-layer graphene	[BMIM] [PF_6]	5.0~6.5	[5] exp
5-layer graphene	6M KOH	2.0~4.0	[6] exp
5-layer graphene	[BMIM] [PF_6]	3.0~4.0	[7] exp
3-layer graphene	[BMIM] [BF_4]	5.5	[8] MD
3-layer graphene	[BMIM] [BF_4]	4.9	[8] MD

Supporting Figures and Captions:

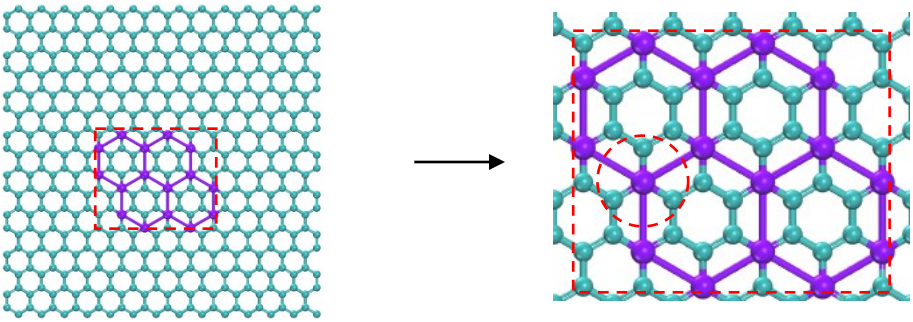

Figure S1. Coarse-grained lattice of graphene. The magnified image shows that each bead in the coarse-grained model represents 4 atoms.

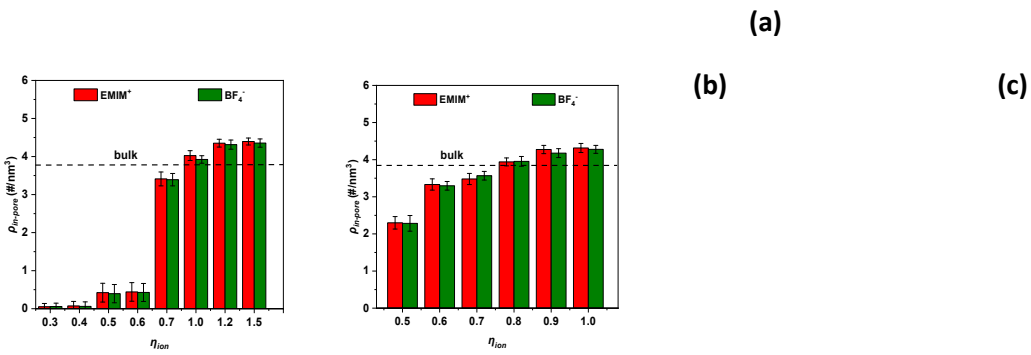

Figure S2. The in-pore ion population at 0 V as a function of the regulated interaction ηion = ε/ε0: (a) 2.46 nm and (b) 3.3 nm. (c) A snapshot of simulation for interface energy calculating. The system consists of a 5-layer graphene base (33.95*33.6 Å) and 130 pairs of EmimBF_4.

Table S3. The specific charge density of different electrodes

U_{ele} (V) \ η_{ion}	0.3	0.5	1.0	1.5
-4.0	-23.7045	-23.0056	-21.5873	-21.8472
-3.5	-20.9756	-20.3887	-19.4409	-19.5904
-3.0	-18.0833	-17.9807	-17.0633	-17.1981
-2.5	-15.0498	-15.1491	-14.5744	-14.3373
-2.0	-12.2647	-12.2089	-11.5392	-11.2671
-1.5	-8.9268	-9.3651	-8.1686	-7.7449
-1.0	-5.4659	-6.2517	-4.9723	-4.9702
-0.5	-2.6005	-2.5982	-2.2153	-2.1523
0.0	0.0000	0.0000	0.0000	0.0000
0.5	2.5999	2.5983	2.2144	2.1538
1.0	5.4662	6.2475	4.9498	4.9768
1.5	8.9279	9.3654	8.1332	7.7509
2.0	12.2654	12.2079	11.5061	11.2678
2.5	15.0534	15.1495	14.5127	14.3386
3.0	18.0871	17.9822	17.0263	17.1994
3.5	20.9817	20.3929	19.4186	19.5912
4.0	23.7110	23.0133	21.6111	21.8573

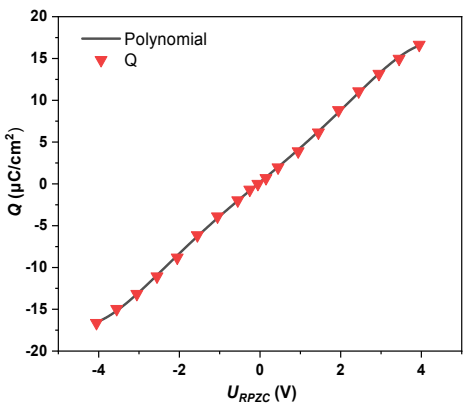

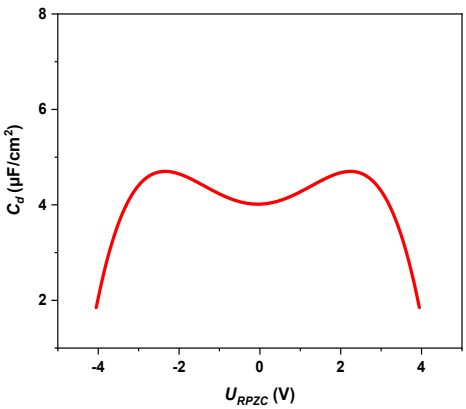

S5

Figure S3. Method to obtain the differential capacitance. (a) The relationship between V_{RPZC} and the electrode surface charge density σ. Points shown as triangles were obtained from simulations, the solid line were the results of the 5-order polynomial fitting. (b) The plot of differential capacitance VS V_{RPZC} obtained from $C_d = dQ/dU_{RPZC}$. The way of obtaining the DC was the same as in several previous work [9, 10]: an order of five polynomial was employed to fit the simulating values of electrode charge density on U_{RPZC} and then the DC was received as the analytical derivative of the fitted polynomial with respect to $U_{RPZC,}$

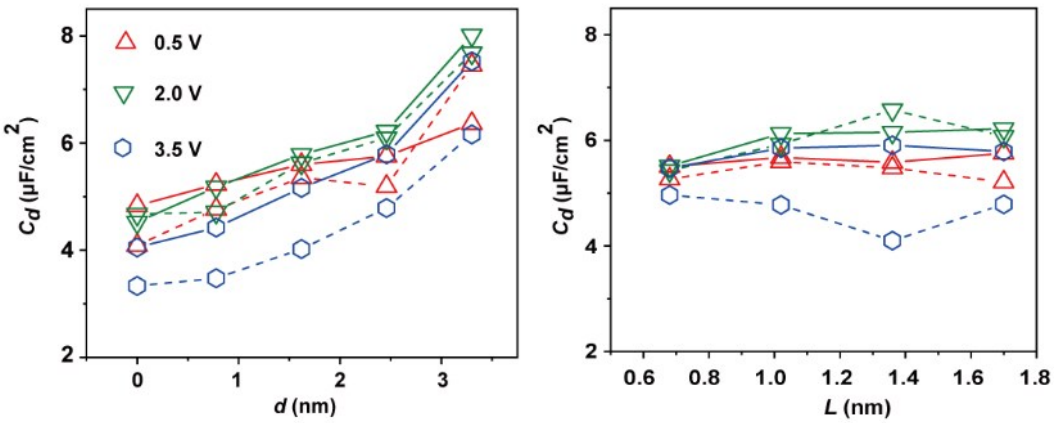

Figure S4. The differential capacitance (U_{RPZC} = 0.5, 2.0, 3.5 V) as a function of the pore size (d) and pore length (L). The solid and dashed lines represent the ionophobic and ionophilic electrode, respectively.

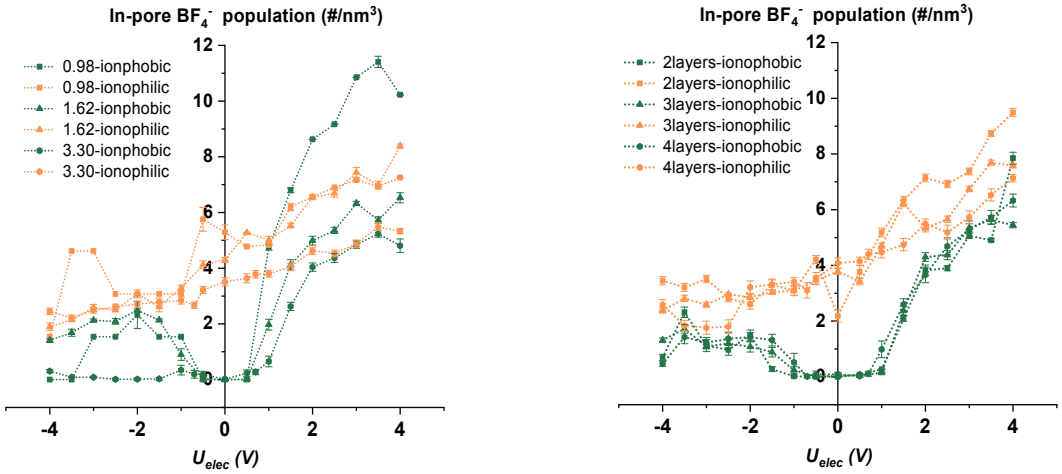

Figure S5. In-pore anion population at different electrodes as a function of the electrical voltage. (a) Porous electrodes with different pore diameters. (b) Porous electrodes with different pore lengths.

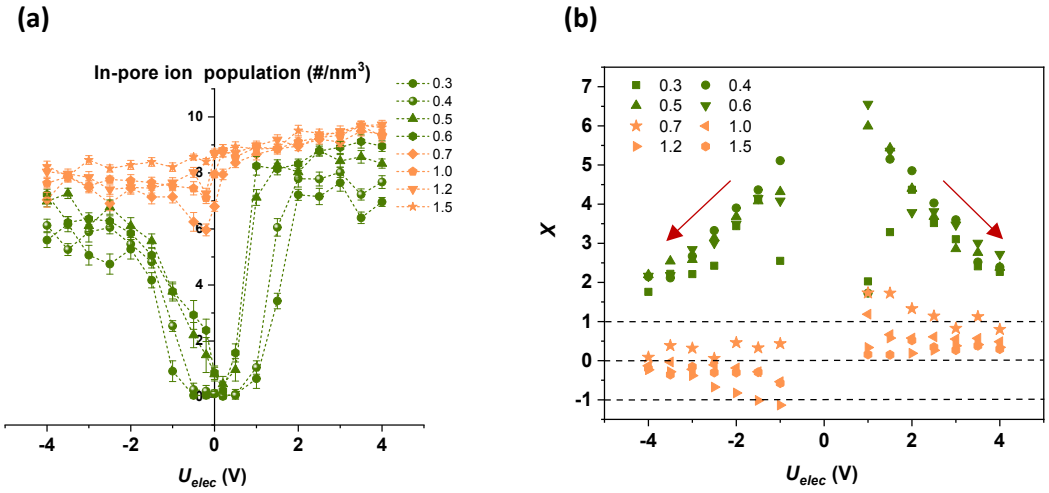

Figure S6. (a) Total number of ions in ionophobic and ionophilic pore at different applied potentials with different coupling strength. (b) Charging mechanism parameters in ionophobic and ionophilic systems at different applied potentials with different coupling strength.

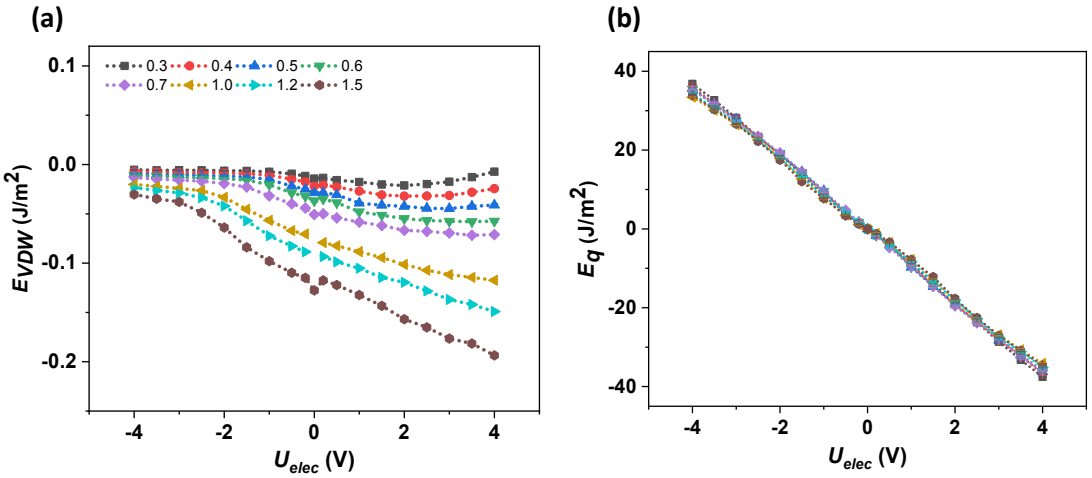

Figure S7. VDW (a) and electrostatic (b) interaction between anion-electrode at different potentials with different coupling strength.

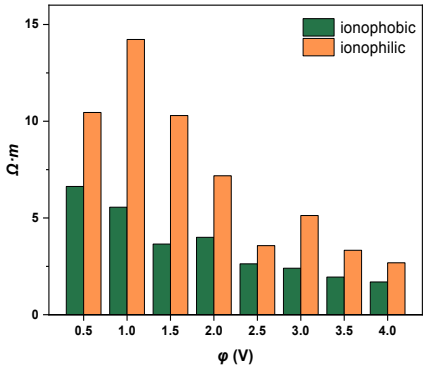

Figure S8. The resistivity of the electrode with ionophobic and ionophilic pore (d_{pore} = 2.46 nm) at different applied potentials.

Supplementary Note S1: Simulation of the equivalent circuit

The resistance of the bulk electrolyte R_{bulk} is derived from the electrical conductivity. First five independent simulations at 298 K were conducted to compute the mean-square displacements (MSDs) and the self-diffusion coefficient was received using the Einstein relation:

$$D_s = \frac{1}{6}\lim_{t\to\infty}\frac{d}{dt}\left\langle \left| r_i(t) - r_i(0) \right|^2 \right\rangle$$

where $r_i(t)$ is the center of mass (COM) position of ion i at time t. Then the conductivity was calculated by Nernst−Einstein (NE) relation:

$$\sigma_{NE} = \frac{N_{pair}}{Vk_BT}\left(q_+^2 D_+ + q_-^2 D_-\right)$$

In the equation, N_{pair} is the number of ion pairs, V the simulation box volume, k_B the Boltzmann constant, and T the temperature. q_+ and q_- are the total charges of the ions (full charges were used), and D_+ and D_- are the self-diffusion coefficients of the cations and anions, respectively. From the simulation, D_+ and D_- are 6.66×10^{-11} m^2/s and 3.51×10^{-11} m^2/s In the end we received the σ=2.418 S m^{-1} and the bulk resistance is $7.25\times10^7\Omega$.

Here we present the analytical results for the charging of the equivalent circuit described in Figure 4 of the manuscript, which are used to analyze the molecular simulation data. From the impedance associated with each component, namely R_{bulk}, R_1, R_2, $1/jC_1\omega$ and $1/jC_2\omega$, and their combination in series and in parallel, the overall impedance of the simulation cell is easily derived as:

$$Z(\omega) = \frac{(j\omega)^2 R_2(R_{bulk}+2R_1)C_1C_2 + j\omega[(R_{bulk}+2R_1)C_1 + (R_{bulk}+2R_1+2R_2)C_2] + 2}{(j\omega)^2 R_2C_1C_2 + j\omega(C_1+C_2)}$$

In Fourier space, the total charge Q of the electrodes is related to the voltage V as:

$$Q(\omega)=\frac{I(\omega)}{j\omega}=\frac{V(\omega)}{j\omega Z(\omega)}$$

where $I(\omega)$ is the intensity.

$$\left[(j\omega)^2+j\omega a+b\right]Q(\omega)=[c+j\omega a]V(\omega)$$

In this equation, the expressions of constants are:

$$a=\frac{(R_{bulk}+2R_1)C_1+(R_{bulk}+2R_1+2R_2)C_2}{R_2(R_{bulk}+2R_1)C_1C_2}$$

$$b=\frac{2}{R_2(R_{bulk}+2R_1)C_1C_2}$$

$$c=\frac{C_1+C_2}{R_2(R_{bulk}+2R_1)C_1C_2}$$

$$d=\frac{1}{R_{bulk}+2R_1}$$

As a result, the total charge *Q*(t) satisfies the following differential equation:

$$Q''(t)+aQ'(t)+bQ(t)=cV(t)+dV'(t)$$

with the same constants *a*, *b*, *c*, *d*. Based on ref [on the dynamics], the solution finally comes to the expression as the manuscript:

$$Q(t)=Q_{max}[1-A_1\exp(-\frac{t}{\tau_1})-A_2\exp(-\frac{t}{\tau_2})]$$

with the following constants:

$$Q_{max}=\frac{c}{b}V_0=\frac{C_1+C_2}{2}V_0$$

$$\tau_1=\frac{2}{a+\sqrt{a^2-4b}}$$

$$\tau_2=\frac{2}{a-\sqrt{a^2-4b}}$$

$$A_1 = \frac{1}{2}[1 + \frac{2bd - ac}{2c\sqrt{a^2 - 4b}}]$$

$$A_2 = \frac{1}{2}[1 - \frac{2bd - ac}{2c\sqrt{a^2 - 4b}}]$$

The charges Q_1 and Q_2 of both slices of the electrode can also be determined from the impedance of each branch of the circuit. The solution for $Q_1(t)$ is then obtained by replacing these coefficients in the solution for $Q(t)$.

Supporting References:

1. E. Paek, A. J. Pak and G. S. Hwang, *J. Electrochem. Soc.*, 2012, **160**, A1-A10.
2. J. Vatamanu, O. Borodin, D. Bedrov and G. D. Smith, *J. Phys. Chem. C*, 2012, **116**, 7940-7951.
3. J. Vatamanu, O. Borodin and G. D. Smith, *J. Am. Chem. Soc.*, 2010, **132**, 14825-14833.
4. J. Vatamanu, O. Borodin and G. D. Smith, *J. Phys. Chem. B*, 2011, **115**, 3073-3084.
5. J. Xia, F. Chen, J. Li and N. Tao, *Nat. Nanotechnol.*, 2009, **4**, 505-509.
6. H. Ji, X. Zhao, Z. Qiao, J. Jung, Y. Zhu, Y. Lu, L. L. Zhang, A. H. MacDonald and R. S. Ruoff, *Nat. Commun.*, 2014, **5**, 3317.
7. E. Uesugi, H. Goto, R. Eguchi, A. Fujiwara and Y. Kubozono, *Sci Rep*, 2013, **3**, 1595.
8. C. Merlet, M. Salanne and B. Rotenberg, *J. Phys. Chem. C*, 2012, **116**, 7687-7693.
9. M. Sha, Q. Dou, F. Luo, G. Zhu and G. Wu, *ACS Appl. Mater. Interfaces*, 2014, **6**, 12556-12565.
10. N. Georgi, A. A. Kornyshev and M. V. Fedorov, *J. Electroanal. Chem.*, 2010, **649**, 261-267.